IOP Publishing Nanotechnology
Nanotechnology 28 (2017) 105301 (9pp) https://doi.org/10.1088/1361-6528/aa596d

Facile design of ultra-thin anodic aluminum oxide membranes for the fabrication of plasmonic nanoarrays

Qi Hao[1,2], Hao Huang[1,2], Xingce Fan[1], Xiangyu Hou[1], Yin Yin[1], Wan Li[2], Lifang Si[1], Haiyan Nan[1], Huaiyu Wang[3], Yongfeng Mei[4], Teng Qiu[1,5] and Paul K Chu[2,5]

[1] Department of Physics, Southeast University, Nanjing 211189, People's Republic of China
[2] Department of Physics and Materials Science, City University of Hong Kong, Tat Chee Avenue, Kowloon, Hong Kong, People's Republic of China
[3] Institute of Biomedicine and Biotechnology, Shenzhen Institutes of Advanced Technology, Chinese Academy of Sciences, Shenzhen 518055, Guangdong, People's Republic of China
[4] Department of Materials Science, Fudan University, Shanghai 200433, People's Republic of China

E-mail: tqiu@seu.edu.cn and paul.chu@cityu.edu.hk

Received 2 November 2016, revised 22 November 2016
Accepted for publication 30 November 2016
Published 31 January 2017

Abstract

Ultra-thin anodic aluminum oxide (AAO) membranes are efficient templates for the fabrication of patterned nanostructures. Herein, a three-step etching method to control the morphology of AAO is described. The morphological evolution of the AAO during phosphoric acid etching is systematically investigated and a nonlinear growth mechanism during unsteady-state anodization is revealed. The thickness of the AAO can be quantitatively controlled from ~100 nm to several micrometers while maintaining the tunablity of the pore diameter. The AAO membranes are robust and readily transferable to different types of substrates to prepare patterned plasmonic nanoarrays such as nanoislands, nanoclusters, ultra-small nanodots, and core–satellite superstructures. The localized surface plasmon resonance from these nanostructures can be easily tuned by adjusting the morphology of the AAO template. The custom AAO template provides a platform for the fabrication of low-cost and large-scale functional nanoarrays suitable for fundamental studies as well as applications including biochemical sensing, imaging, photocatalysis, and photovoltaics.

Supplementary material for this article is available online

Keywords: plasmonic nanoarrays, three-step etching, melt infiltration, shadow deposition, template assisted nano-patterning, anodic aluminum oxide

(Some figures may appear in colour only in the online journal)

Introduction

Template assisted nano-patterning, an effective strategy for high-throughput fabrication of nanoarchitectures with precise structural control and good reproducibility, has been applied to prepare metal, semiconductor, polymer and carbon nanoarrays ranging from dots, rings, pillars and tubes to pores, holes and meshes [1–7] for photovoltaics [8, 9], nanolasers [10] and chemical and biological analyses [11, 12]. Compared to the serial writing process in electron beam lithography [13–15], this low-cost technique is suitable for large-scale nanofabrication as well as preparation of ultra-small nanostructures due to the high resolution down to 10 nm [16, 17].

The anodic aluminum oxide (AAO) membrane is one of the most common nanotemplates for the preparation of

[5] Authors to whom any correspondence should be addressed.

multifunctional nanomaterials [11, 18–20]. In particular, ultra-thin AAO films can be transferred onto different types of substrates to produce nanoparticle arrays with variable particle diameters from 15–400 nm and interparticle spacings from 50–400 nm [21–29]. However, the use of AAO membranes in template-assisted nano-patterning is not yet well developed due to the difficulty in controlling the AAO film thickness/aspect ratio precisely. The difficulty originates from the unsteady-state growth of ultra-thin AAO and intractability in manipulation. Besides, modulation of the AAO pore diameter by chemical etching always leads to variations in the film thickness. Efforts have been made to circumvent these difficulties, for example, by growing a barrier layer-free AAO directly on conductor-coated substrates [30]. However, fabrication of layer-free AAO is only applicable to specific substrates and so the full potential of AAO membranes has not yet been realized.

The film thickness of a stencil mask is vital to the production of customized nanoarrays. For example, precise control of the film thickness is required in electrochemical deposition to fabricate nanowires, nanorods, and nanotubes with the desired thickness. Besides, the pore length-width ratio is essential when using nanomasks in shadow deposition to produce complex superstructures [31–35]. Herein, a three-step etching method to address the aforementioned problems is designed and described. This method enables selective etching of specific areas on the AAO membrane and consequently, the membrane thickness can be continuously and quantitatively reduced to 80 nm while the AAO pore diameter is maintained. The protocol is demonstrated by the fabrication of patterned plasmonic nanoarrays with various morphologies including nanoclusters, nanoislands, ultra-small nanodots, and hetero core–satellites structures as well as modulation of the plasmonic modes.

Methods

Preparation of the ultra-thin AAO membrane

The AAO membrane was formed on an aluminum foil (99.999%, 0.2 mm in thickness) by using the two-step anodization method [36]. The aluminum foil was degreased with acetone, annealed at 400 °C for 30 min under vacuum to remove mechanical stress, and electropolished in a 1:4 solution of perchloric acid and ethanol at 15 V for 5 min. The first anodization was performed by applying a DC voltage of 40 V in 0.3 M oxalic acid at 0 °C for 12 h. The thermometer was placed near the surface of the AAO film during anodization to measure the temperature accurately. The alumina formed in the first anodization process was dissolved by chemical wet etching in a solution of phosphoric acid (6 wt%) and chromic acid (1.8 wt%) with a volume ratio of 1:1 at 75 °C for 2 h. The aluminum foil was subjected to a DC voltage of 40 V in the same solution as the first anodization step but for short anodization time to produce the ultra-thin AAO membrane. After the second anodization step, the AAO membrane was immersed in 5 wt% phosphoric acid at 30 °C to perform top etching. The AAO was spin-coated with a PMMA layer (950PMMA A4 from MicroChem) at 600 rpm for 8 s and 3000 rpm for 60 s (Laurell spin coater WS-400BZ-6NPP-Lit). The PMMA/AAO membrane was annealed at 250 °C for 2 h to form an AAO membrane with PMMA filling the pores. The remaining aluminum foil was etched by fixing the sample at the bottom in a $CuCl_2$ solution. In our experiments, the concentration of $CuCl_2$ solution was limited to 100 g l^{-1} to avoid violent reaction. In addition, 200 ml $CuCl_2$ solution was appropriate for an aluminum foil with dimensions of 30 mm × 30 mm × 0.2 mm. Removal of the AAO barrier layer and bottom etching were carried out in a 5 wt% phosphoric acid solution. Finally, the PMMA layer was dissolved in acetone and then the remaining AAO membrane was rinsed with distilled water for several times and transferred onto the desired substrate. It should be noted that AAO membranes broke during the rinsing if there was excessive acetone on the sample or the acetone is totally evaporated.

Preparation of plasmonic nanoarrays by electron beam evaporation

Ag and Al was evaporated onto the AAO coated substrates by electron beam evaporation at 8×10^{-4} Pa at a rate of 0.15 nm s^{-1}. The film thickness was measured by a film-thickness monitor (Taiyao FTM-V). After evaporation, the AAO membrane was stripped with a tape leaving the ordered plasmonic nanoarrays. The shadow deposition was conducted by placing the AAO membranes bottom up on the substrate to let the protuberance structures of AAO in contact with the substrate. Here the AAO membranes were anodized for 10 min with $t_1 = 20$ min, $t_2 = 25$ min, $d = 65$ nm and $h = 260$ nm, respectively. In the first evaporation, 60 nm thick silver nanoislands were fabricated at the central locations of the AAO pores. Then the second evaporation was conducted by placing the AAO membranes with an incident angle α to the evaporation direction to produce the satellites. The AAO membranes were placed 8 cm off the vertical center of the evaporation source to change the incident angle and the vertical evaporation distance was 30 cm. The value of the incident angle α was calculated based on the aspect ratio of the AAO. The AAO membrane were kept rotating during the second evaporation and finally hetero core–satellites structures were fabricated.

Instrumentation and data acquisition

The scanning electron microscopy images were acquired on the field-emission scanning electron microscope (FE-SEM, FEI Inspect F50). The UV–visible absorption spectra were acquired from a PerkinElmer LAMBDA 750 spectrophotometer and ImageJ software version 1.48 was used to conduct the statistical analysis of the nanoparticle scale. The Raman scattering spectra were collected on a Jobin Yvon LabRAM HR800 micro-Raman spectrometer equipped with a 514 nm wavelength argon ion laser. The cumulative exposure time was 5 s and laser power density was about 5×10^7 mW cm^{-2}. The substrate was maintained for 30 min in the 10^{-7} M Rhodamine

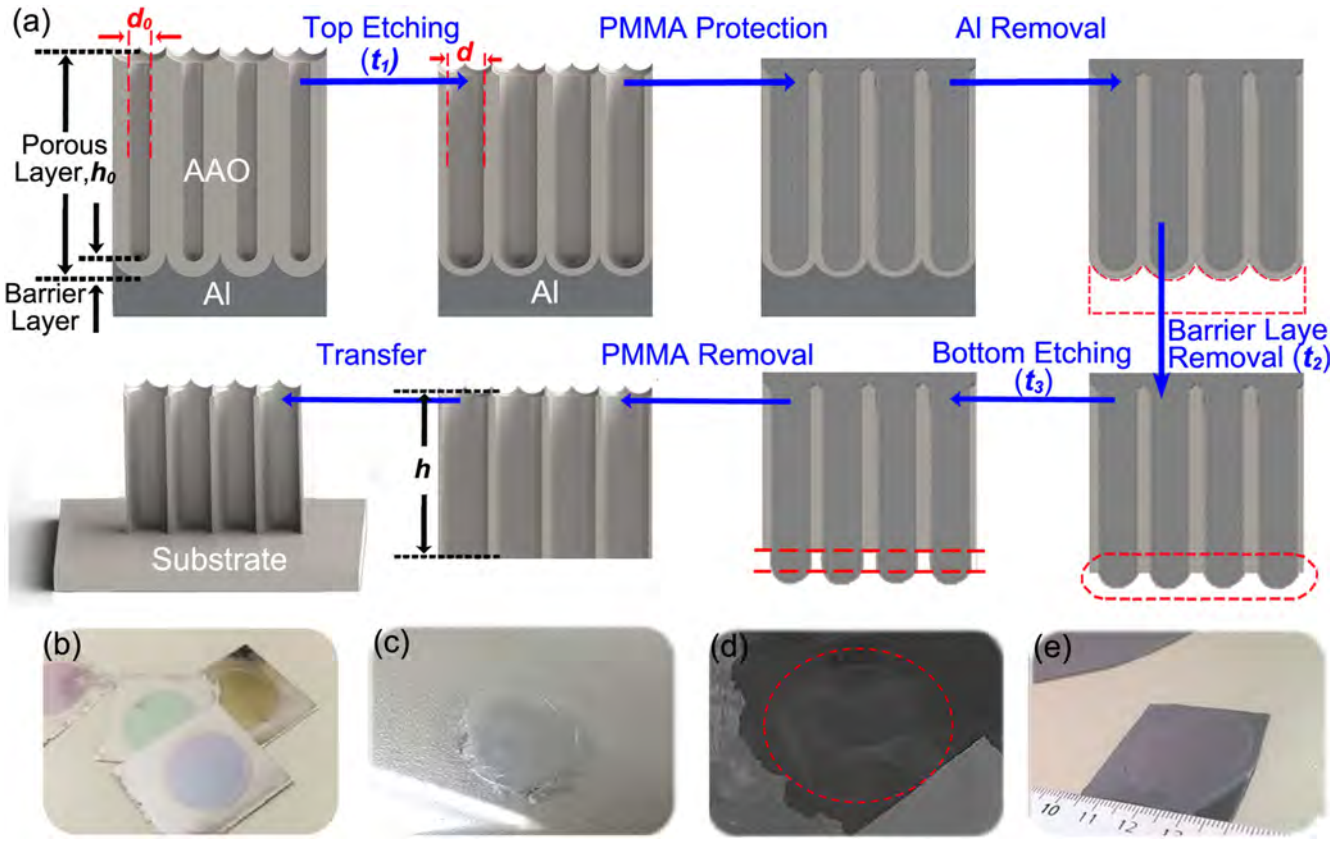

Figure 1. (a) Schematic illustration of the preparation of ultra-thin AAO membranes by the three-step etching method. Optical photos of AAO membranes: (b) fabricated on aluminum foils for different anodization time, (c) floating on water after removal of aluminum foils, (d) tumbling in acetone when removing PMMA, and (e) transferred onto a silicon wafer substrate.

6G solution and then taken out and rinsed thoroughly for Raman analysis. Baseline correction was performed to remove the background and fluorescence signal and the EF was calculated using a standard formula [37].

Results and discussion

Figure 1(a) illustrates the fabrication of the ultra-thin AAO membrane by the three-step etching method. The process begins with a typical anodization method [38] in which the initial film thickness of the AAO, h_0, is determined by the anodization time. The variation in h_0 leads to different color which can be used to roughly gauge the film thickness, as shown in figure 1(b). The AAO is composed of a close-packed array of hexagonal cells, each containing six protuberances at the vertex of the hexagonal cell and a cylindrical central pore which extends down to the alumina barrier layer between the pore bottom and Al foil. After anodization, top etching is conducted by immersing the AAO in a phosphoric acid solution to enlarge the pore diameter, d, and reduce the film thickness, h. Afterwards, the AAO surface is spin-coated with a PMMA protective layer on top of the AAO pore. However, routine spin coating cannot offer efficient protection of the AAO membrane thereby leading to unavoidable enlargement in d when adjusting h in subsequent etching procedures. In this study, melt infiltration is adopted to melt the PMMA layer into the AAO nanopores at 250 °C for 2 h by considering the molecular weight of the PMMA and its glass transition temperature [39–43]. More detailed information about the melt infiltration method and performance of the PMMA protection layer are described in the online supplementary data is available online at stacks.iop.org/NANO/28/105301/mmedia. The PMMA layer provides complete coverage of the surface of the AAO pores and protects the membrane enabling continuous tuning of h in the ensuing etching procedures while d is fixed. After melt infiltration, the remaining aluminum foil is removed in a $CuCl_2$ solution. After the aluminum is removed completed, the PMMA/AAO membrane is automatically outstretched on water by surface tension as shown in figure 1(c). The membrane is then rinsed in water and transferred to a phosphoric acid solution to etch the barrier layer while h is further adjusted to the desired value during subsequent bottom etching. After etching, the PMMA layer is dissolved in acetone and the ultra-thin AAO membrane exhibits a flexible characteristic and keeps fluctuating in acetone as shown in figure 1(d). Finally, the intact AAO membrane is rinsed with distilled water and transferred to the substrate of choice. Figure 1(e) shows that the diameter of the AAO membrane is 2.5 cm and larger samples can be prepared by using bigger anodization equipment.

The three-step etching method provides precise control of the AAO morphological parameters. Here, t_1 is the top etching time, t_2 is the barrier layer removal time, t_3 is the

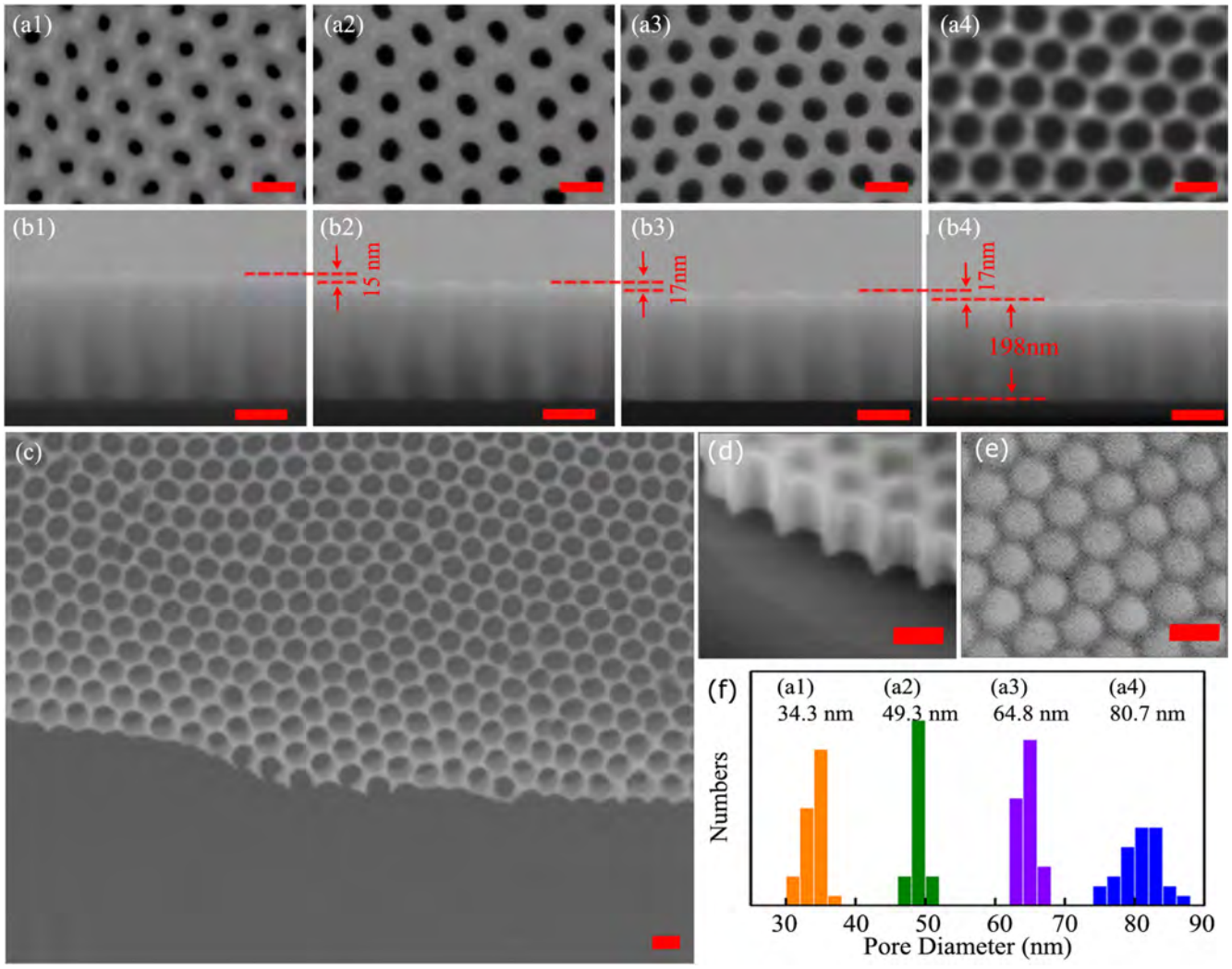

Figure 2. SEM characterization of the ultra-thin AAO membrane. (a1)–(a4) AAO pore widening by increasing the top etching time, $t_1 = 0$ min, 10 min, 20 min, and 30 min, respectively. (b1)–(b4) AAO membranes with tunable film thickness by adopting a different bottom etching procedure. The AAO in (b1–b4) is anodized for 10 min for $t_1 = 20$ min, $t_2 = 25$ min, and $t_3 = 0$ min, 10 min, 20 min, and 30 min, respectively. (c), (d) Large-area SEM image of an ultra-thin AAO membrane and corresponding SEM image at 45°. (e) Bottom view of the AAO membrane with the barrier layer. (f) Calculated scale distribution of the pore diameter in (a1)–(a4). The scale bars in the SEM images are 100 nm.

bottom etching time, and t is the total etching time. Here, t_1 controls d and t determines h, as shown in figure 2. Figures 2(a1)–(a4) shows the SEM images of the AAO membranes revealing that d can be continuously tuned from 35 to 80 nm by adjusting t_1. The distribution of d in figures 2(a1)–(a4) is presented in figure 2(f), showing that d is enlarged at a rate of $\nu_d = 1.5\ \text{nm min}^{-1}$ during top etching. Figures 2(b1)–(b4) reveals the thickness variation of AAO during bottom etching and it is clear that d can be maintained while h decreases at a rate of $\nu_h = 1.6 \pm 0.2\ \text{nm min}^{-1}$. Besides, ν_h is measured in the top etching and barrier layer removal procedures and there is no significant difference as illustrated in online supplementary figure S1. The empirical equations based on our experiments results are provided to estimate d and h:

$$d = d_0 + \nu_d\, t_1 \quad (1)$$

$$h = h_0 - \nu_h\, t, \quad (2)$$

where d_0 presents the initial diameter of the AAO pore. The measured ν_h is larger than the transversal etching rate $\nu_d/2$ probably due to the morphological difference. Figures 2(c)–(e) present the well-defined hexagonal structure of the ultra-thin AAO membranes fabricated by three-step etching. The minimum thickness can be adjusted down to ~100 nm and the corresponding AAO film is almost transparent as shown in online supplementary figure S2.

To study the growth mechanism of the ultra-thin AAO, the second anodization process is repeated for about 100 times at 0 °C and the current density versus anodization time curves are plotted in figure 3(a). During anodization, there are three main stages as shown by the current density curve [44]. In stage (I), a compact barrier oxide layer starts to grow quickly in several seconds on the aluminum surface giving rise to sharp decrease in the current. In stage (II), the initial barrier oxide thickens leading to increased series resistance in the anodization circuit. When the thickness of the barrier layer reaches a certain value,

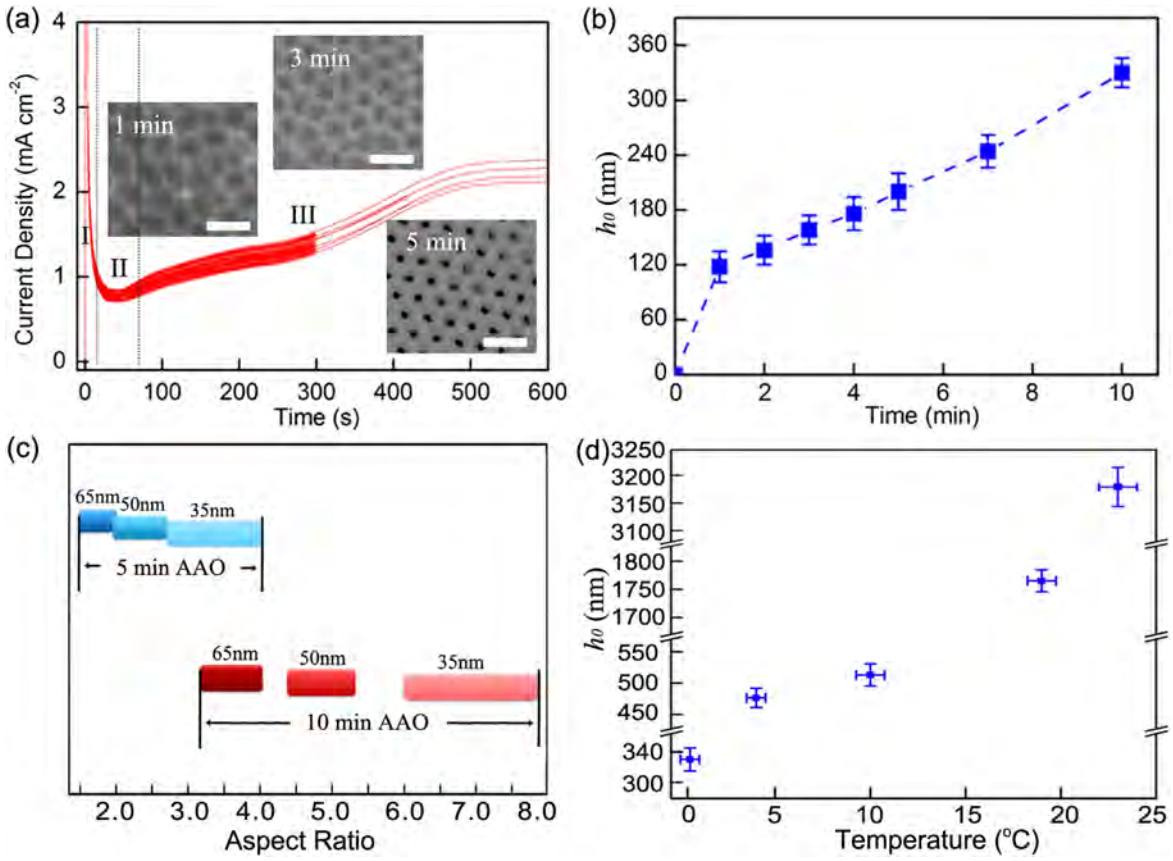

Figure 3. Characteristics of the ultra-thin AAO membrane: (a) AAO current density–time curves at 0 °C and corresponding SEM images of AAO with a different anodization time. (b) Relationship between the AAO initial film thickness, h_0, and anodization time. (c) Aspect ratio tuning of the AAO anodized for 5 min (h_0 = 200 nm) and 10 min (h_0 = 330 nm) with d = 35 nm, 50 nm and 65 nm. (d) Initial film thickness, h_0 of the AAO membrane anodized for 10 min at different temperature. The scale bars in the SEM images are 200 nm.

the current density drops rapidly to a minimum value. Then the electric field concentrates on local imperfections on the initial barrier oxide, resulting in non-uniform oxide thickening and development of individual penetration paths into the initial pores [45]. As time elapses (stage III), the current increases gradually and the pores grow in size by merging with adjacent ones. In this stage, the major pores morph into a stable U-shape and the current reaches a steady-state slowly. Evolution of AAO surface morphology during anodization is revealed by the SEM images in figures 3(a) and online supplementary S2. Steady-state growth occurs in stage IV, but it is indistinguishable experimentally at 0 °C as shown in online supplementary figure S3. In the entire anodization process, h_0 is almost linearly proportional to the total amount of charge involved in the electrochemical reaction [19]. Hence, it can be deduced that the growth rate in the first few minutes is very unstable based on the current density curves. According to SEM, h_0 increases nonlinearly with time in the first 10 min as shown in figure 3(b). The growth rate decreases quickly reaching a minimum after one minute and then increases gradually to 28 nm min^{-1} after 10 min. Since h can be continuously varied in bottom etching while keeping d constant, the aspect ratio of the AAO can be conveniently tuned by adopting the appropriate anodization time and optimizing the etching procedures. The tuning range of AAO aspect ratio is illustrated by the bar charts in figure 3(c) which is plotted based on the supporting data set in online supplementary table S1. The results show that a minimum aspect ratio of 1.2 can be obtained. Additionally, h_0 can be tuned by adjusting the anodization temperature to obtain thicker AAO membranes, as illustrated in figure 3(d). The corresponding current density versus time curves are shown in online supplementary figure S3.

Anodization of the ultra-thin AAO usually takes less than 10 min and it is different from the steady-state AAO that requires several hours. The differences are systematically compared in table 1. In the initial stage, the barrier layer is thicker than that in the steady state. The dynamic barrier layer thickness results in dramatic variation in the electric field distribution on the oxide. As a result, the current density and film growth rate are unstable in the first 10 min. When the anodization current reaches a steady state, the thickness of the barrier layer is fixed and directly proportional to the applied potential [46]. Besides the barrier layer thickness, the interpore distance in the steady state is also linearly proportional to the anodizing potential [47]. When the AAO is anodized in 0.3 M $H_2C_2O_4$ at 0 °C and 40 V, it takes at least 5 min to form the patterned hexagonal array with the interpore distance and pore diameter close to those in the steady state. The shorter anodization time leads to non-uniform interpore distance and randomly distributed pore structures as

Table 1. Ultra-thin AAO versus steady state AAO in 0.3 M $H_2C_2O_4$ at 0 °C.

	Ultra-thin at 1 min	Ultra-thin at 10 min	Steady state at 2 h
Barrier layer thickness-to-voltage ratio (nm V^{-1})	>1.3	1.3	1.3 [46]
Current density (mA cm^{-2})	0.83	2.05	1.8 (figure S3)
Average film growth rate (nm min^{-1})	~120	~28	32 (figure S3) [18]
Interpore distance-to-voltage ratio (nm V^{-1})	2.2–4.3	2.5	2.5 [47]
Pore diameter (nm)	N/A	35	35 (figure 2)

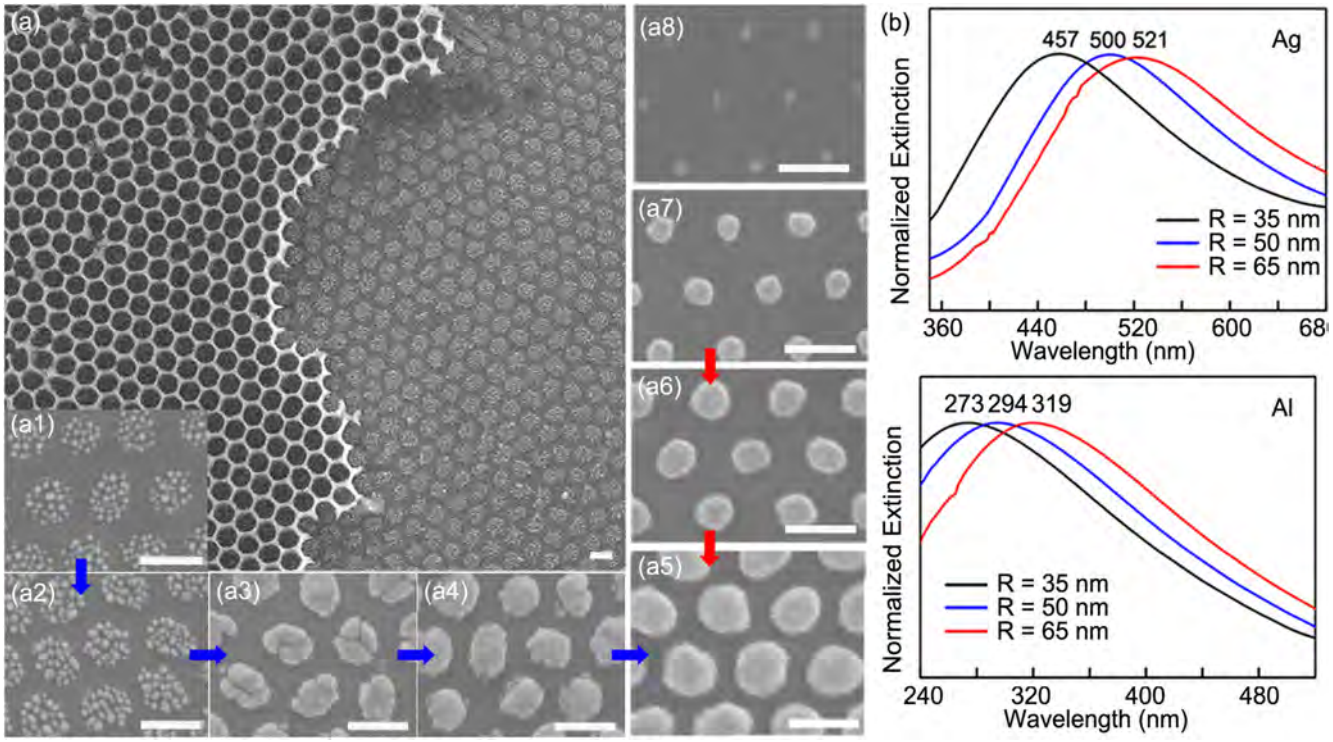

Figure 4. Fabrication of plasmonic nanoarrays by adopting the AAO membranes as masks: (a) SEM images of the patterned plasmonic nanoarrays fabricated by electron evaporation utilizing ultra-thin AAO as masks. The large-area SEM image exhibits the patterned silver cluster nanoarray fabricated with a ~100 nm thick AAO mask. (a1)–(a5) Evolution of the plasmonic nanoarrays during evaporation with a layer thickness of 5 nm, 10 nm, 20 nm, 40 nm, and 60 nm, respectively. (a5)–(a7) 60 nm thick metallic nanoislands fabricated by adopting the AAO masks with d = 65 nm, 50 nm and 35 nm, respectively. (a8) Ultra-small nanodots fabricated by partial removal of the AAO barrier layer and the etching time for the AAO mask is t_1 = 1200 s and t_2 = 1400 s. (b) UV–vis spectra of the Ag and Al plasmonic arrays from (a5)–(a7) on the quartz substrate. The scale bars in the SEM images are 100 nm.

depicted in figure 3(a). Based on the results, the minimum oxidation time is 5 min (h_0 = 200 nm) in order to ensure the patterns of the fabricated AAO membrane.

The AAO membrane serves as the template to prepare customized plasmonic nanoarrays by electron beam evaporation and the results are displayed in figure 4. Figures 4(a1)–(a5) disclose that electron beam evaporation generates nanocluster structures when the thickness is less than 10 nm and then the clusters merge into nanoislands afterwards. The large-area SEM image in figure 4(a) shows the regularity of the AAO membrane which ensures the homogeneity of the fabricated plasmonic arrays. The versatility of the AAO membrane allows the fabrication of plasmonic nanostructures with customized size and shape so that tunable plasmonic modes with different characteristics can be achieved [48–50]. Figures 4(a5)–(a7) display the SEM images of the 60 nm thick silver nanoisland arrays with different diameters by tuning d in the top etching process. There is no obvious difference in the SEM images when the metal is changed to aluminum. The UV–vis spectra in figure 4(b) show that the variations in d lead to redshifts in the corresponding plasmonic bands. The redshifts originating from the phase delay across the nanoparticles [51] can be utilized in sensing and imaging applications by coupling the plasmonic bands with the electromagnetic wave of the excitation. The SEM results in figure 4(a8) shows ultra-small nanodots with a quantum size of 12 ± 2 nm and more SEM images are available in online supplementary figure S4. The ultra-small nanodots are fabricated by controlling t_2 to partially remove the AAO barrier layer and vary the scale of the AAO bottom diameter. During the barrier layer removal process, the bottom diameter of AAO broadens very quickly so that precise control over t_2 is vital to the size scale. Fabrication of quantum-size nanoparticles with the AAO mask

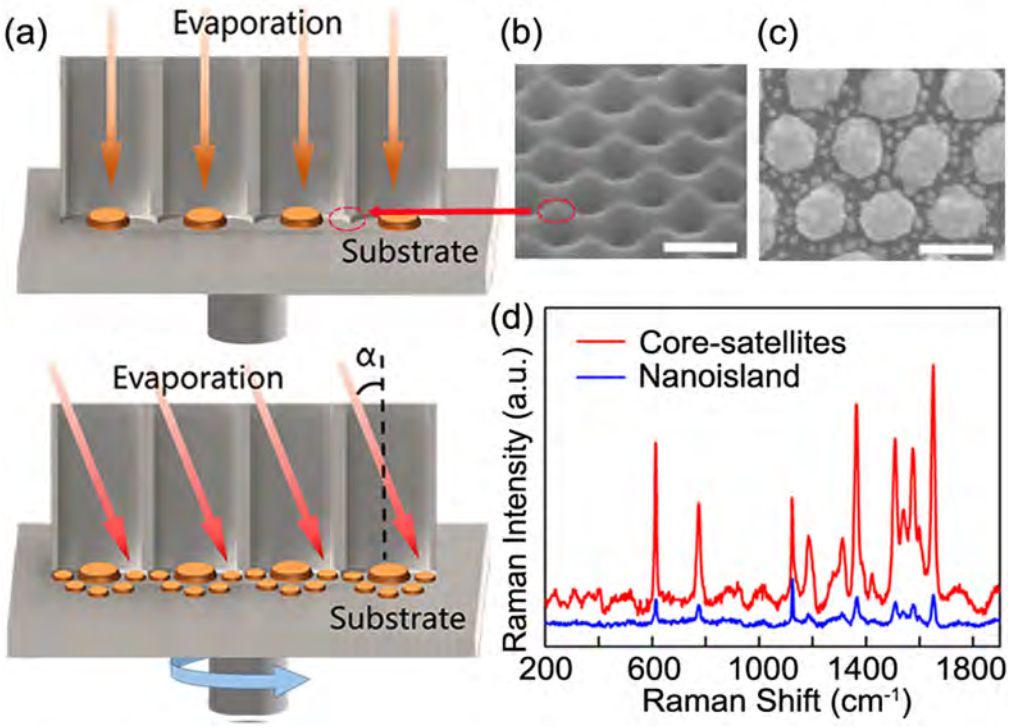

Figure 5. (a) Schematic of the fabrication of the hetero core–satellites structures by shadow deposition with an AAO mask. (b) 45° angle SEM image of the protuberance structures on AAO surface. (c) SEM image of the fabricated hetero core–satellites structures. (d) SERS spectra of 10^{-7} M Rhodamine 6 G molecules on nanoislands in figure 4(a5) and on hetero core-satellites. The scale bars are 100 nm.

used to be difficult because the regularity of pores is poor when d_0 is smaller than 20 nm, although efforts have been made by using specific electrolytes or smaller anodization voltage and a pore diameter of 15 nm has been reported [16, 29, 52]. Here, surface patterning of quantum-size nanodots down to 12 nm is realized for the first time. Nanoparticles with reduced size offer the opportunity to study the quantum confinement effect where the plasmon resonance is more sensitive to the quantum nature of the conduction electrons. In addition, quantum-size particles can improve nanoparticle integration and increase the surface-to-volume ratios thereby to the benefit of applications of imaging, sensing and catalysis as well as novel quantum devices [53].

Controlled assembly of complex plasmonic nanostructures into organized superstructures is a great scientific and technological challenge. Molecular-linker mediated assembly methods have been proposed to induce the formation of core–satellites hetero-assemblies, but these assemblies are not stable in ensuing chemical and biological functionalization [54]. Here, we present a new method to fabricate large-scale and patterned hetero core–satellites nanostructures by utilizing the protuberance structures of AAO and shadow deposition as shown in figure 5(a). The AAO membrane with $d = 65$ nm and $h = \sim 260$ nm is placed bottom up on the substrate to let the top surface with protuberance (figure 5(b)) in closely contact with the substrate. The protuberance structures undergoing different top etching are shown in online supplementary figure S5. The gap between the AAO protuberances provide the extra space on the interstitial locations of the protuberances, where small nanodots can be fabricated by optimizing the evaporation angle α. Details about the shadow evaporation method is described in the experimental section. In the fabricated core–satellites nanoarray, each unit consists of a central nanoisland particle with a diameter of ~65 nm and several surrounding satellite particles with a diameter of ~10 nm, as shown in figure 5(c). When the core and satellites are in close proximity, the strong coupling originating from the high density of sub-10 nm interparticle gaps can support extremely intense local electromagnetic fields to the benefit of surface-enhanced Raman scattering (SERS). Figure 5(d) displays the SERS signal of Rhodamine 6 G molecules from the silver nanoisland array in figure 4(a5) and core–satellites array in figure 5(b). While the individual nanosislands typically produce modest SERS, the plasmonic core–satellites nanostructures exhibit a cascade SERS signal with an enhancement factor (EF) of up to 10^9. The result is calculated from the expression $EF = (I_{Surface}/I_{Ref}) \times (N_{Ref}/N_{surface})$ [37]. In addition, SERS spectra as a function of the R6G concentration and Raman maps revealing the signal uniformity are shown in figure S6. The results illustrate that the combination of AAO mask and shadow deposition provide the platform to design and prepare complex metamaterials for ultrasensitive chemical and biological detection and sensing.

Conclusion

A three-step etching method is developed to prepare ultra-thin AAO membranes without breaking the integrity and a

nonlinear growth mechanism is demonstrated. Since transversal and longitudinal etching of the AAO in phosphoric acid is independent of each other, this technique enables the design and preparation of AAO membranes with tunable core diameter and desired thickness down to 100 nm and modulation of metallic nanoarrays with tunable plasmonic bands. Ultra-small nanodots with a quantum size of 12 nm are demonstrated and hetero core-satellites superstructures are produced. Boasting desirable features such as large-area fabrication, self-ordered arrays, optical tunability and manufacturability of complex metamaterials, the three-step etching method can be utilized to fabricate custom plasmonics nanoarrays to investigate light–matter interactions and form highly sensitive sensing platforms. This approach can be readily extended to the fabrication of patterned nanoparticles, nanowires, nanorods, and nanotubes of various materials including polymers, carbon materials, and semiconductors.

Acknowledgments

The authors thank Professor Zhenhua Ni for valuable discussion. TQ acknowledges support from the National Natural Science Foundation of China under Grant No. 51271057. PKC acknowledges City University of Hong Kong Applied Research Grant (ARG) No. 9667122 as well as Strategic Research Grant (SRG) No. 7004644.

References

[1] Kosiorek A, Kandulski W, Glaczynska H and Giersig M 2005 Fabrication of nanoscale rings, dots, and rods by combining shadow nanosphere lithography and annealed polystyrene nanosphere masks *Small* **1** 439–44

[2] Schierhorn M, Boettcher S W, Kraemer S, Stucky G D and Moskovits M 2009 Photoelectrochemical performance of CdSe nanorod arrays grown on a transparent conducting substrate *Nano Lett.* **9** 3262–7

[3] Zhang J H, Li Y F, Zhang X M and Yang B 2010 Colloidal self-assembly meets nanofabrication: from two-dimensional colloidal crystals to nanostructure arrays *Adv. Mater.* **22** 4249–69

[4] Zeng Z *et al* 2012 Fabrication of graphene nanomesh by using an anodic aluminum oxide membrane as a template *Adv. Mater.* **24** 4138–42

[5] Halpern A R and Corn R M 2013 Lithographically patterned electrodeposition of gold, silver, and nickel nanoring arrays with widely tunable near-infrared plasmonic resonances *ACS Nano* **7** 1755–62

[6] Saboktakin M, Ye X C, Chettiar U K, Engheta N, Murray C B and Kagan C R 2013 Plasmonic enhancement of nanophosphor upconversion luminescence in Au nanohole arrays *ACS Nano* **7** 7186–92

[7] Karimullah A S *et al* 2015 Disposable plasmonics: plastic templated plasmonic metamaterials with tunable chirality *Adv. Mater.* **27** 5610–6

[8] Nakayama K, Tanabe K and Atwater H A 2008 Plasmonic nanoparticle enhanced light absorption in GaAs solar cells *Appl. Phys. Lett.* **93** 121904

[9] Yu B, Goodman S, Abdelaziz A and O'Carroll D M 2012 Light-management in ultra-thin polythiophene films using plasmonic monopole nanoantennas *Appl. Phys. Lett.* **101** 151106

[10] Yang A K *et al* 2015 Unidirectional lasing from template-stripped two-dimensional plasmonic crystals *ACS Nano* **9** 11582–8

[11] Jani A M M, Losic D and Voelcker N H 2013 Nanoporous anodic aluminium oxide: advances in surface engineering and emerging applications *Prog. Mater. Sci.* **58** 636–704

[12] Abdulhalim I 2014 Plasmonic sensing using metallic nano-sculptured thin films *Small* **10** 3499–514

[13] Abu Hatab N A, Oran J M and Sepaniak M J 2008 Surface-enhanced Raman spectroscopy substrates created via electron beam lithography and nanotransfer printing *ACS Nano* **2** 377–85

[14] Near R, Tabor C, Duan J, Pachter R and El-Sayed M 2012 Pronounced effects of anisotropy on plasmonic properties of nanorings fabricated by electron beam lithography *Nano Lett.* **12** 2158–64

[15] Dong Z G *et al* 2015 Second-harmonic generation from sub-5 nm gaps by directed self-assembly of nanoparticles onto template-stripped gold substrates *Nano Lett.* **15** 5976–81

[16] Malinovskis U *et al* 2014 Ultrathin anodic aluminum oxide membranes for production of dense sub-20 nm nanoparticle arrays *J. Phys. Chem.* C **118** 8685–90

[17] Zhang M *et al* 2015 High-density 2D homo- and hetero-plasmonic dimers with universal sub-10 nm gaps *ACS Nano* **9** 9331–9

[18] Lee W, Ji R, Gösele U and Nielsch K 2006 Fast fabrication of long-range ordered porous alumina membranes by hard anodization *Nat. Mater.* **5** 741–7

[19] Lee W and Park S-J 2014 Porous anodic aluminum oxide: anodization and templated synthesis of functional nanostructures *Chem. Rev.* **114** 7487–556

[20] Kumeria T, Santos A and Losic D 2014 Nanoporous anodic alumina platforms: engineered surface chemistry and structure for optical sensing applications *Sensors* **14** 11878–918

[21] Masuda H and Satoh M 1996 Fabrication of gold nanodot array using anodic porous alumina as an evaporation mask *Japan. J. Appl. Phys.* **35** L126

[22] Lei Y, Cai W and Wilde G 2007 Highly ordered nanostructures with tunable size, shape and properties: a new way to surface nano-patterning using ultra-thin alumina masks *Prog. Mater. Sci.* **52** 465–539

[23] Lee W *et al* 2008 Individually addressable epitaxial ferroelectric nanocapacitor arrays with near Tb inch-2 density *Nat. Nanotechnol.* **3** 402–7

[24] Lei Y, Yang S, Wu M and Wilde G 2011 Surface patterning using templates: concept, properties and device applications *Chem. Soc. Rev.* **40** 1247–58

[25] Al-Haddad A, Zhan Z, Wang C, Tarish S, Vellacheria R and Lei Y 2015 Facile transferring of wafer-scale ultrathin alumina membranes onto substrates for nanostructure patterning *ACS Nano* **9** 8584–91

[26] Li A, Müller F, Birner A, Nielsch K and Gösele U 1998 Hexagonal pore arrays with a 50–420 nm interpore distance formed by self-organization in anodic alumina *J. Appl. Phys.* **84** 6023–6

[27] Belwalkar A, Grasing E, Van Geertruyden W, Huang Z and Misiolek W 2008 Effect of processing parameters on pore structure and thickness of anodic aluminum oxide (AAO) tubular membranes *J. Membr. Sci.* **319** 192–8

[28] Poinern G E J, Ali N and Fawcett D 2011 Progress in nano-engineered anodic aluminum oxide membrane development *Materials* **4** 487–526

[29] Martín J, Manzano C V, Caballero-Calero O and Martín-González M 2012 High-aspect-ratio and highly ordered 15 nm porous alumina templates *ACS Appl. Mat. Inter.* **5** 72–9

[30] Sander M S and Tan L S 2003 Nanoparticle arrays on surfaces fabricated using anodic alumina films as templates *Adv. Funct. Mater.* **13** 393–7
[31] Masuda H, Yasui K and Nishio K 2000 Fabrication of ordered arrays of multiple nanodots using anodic porous alumina as an evaporation mask *Adv. Mater.* **12** 1031–3
[32] Kosiorek A, Kandulski W, Chudzinski P, Kempa K and Giersig M 2004 Shadow nanosphere lithography: simulation and experiment *Nano Lett.* **4** 1359–63
[33] Fredriksson H *et al* 2007 Hole-mask colloidal lithography *Adv. Mater.* **19** 4297–302
[34] Nemiroski A, Gonidec M, Fox J M, Jean-Remy P, Turnage E and Whitesides G M 2014 Engineering shadows to fabricate optical metasurfaces *ACS Nano* **8** 11061–70
[35] Ogier R, Shao L, Svedendahl M and Käll M 2016 Continuous-gradient plasmonic nanostructures fabricated by evaporation on a partially exposed rotating substrate *Adv. Mater.* **28** 4658–64
[36] Qiu T, Zhang W, Lang X, Zhou Y, Cui T and Chu P K 2009 Controlled assembly of highly Raman-enhancing silver nanocap arrays templated by porous anodic alumina membranes *Small* **5** 2333–7
[37] Cho W J, Kim Y and Kim J K 2011 Ultrahigh-density array of silver nanoclusters for SERS substrate with high sensitivity and excellent reproducibility *ACS Nano* **6** 249–55
[38] Masuda H and Fukuda K 1995 Ordered metal nanohole arrays made by a two-step replication of honeycomb structures of anodic alumina *Science* **268** 1466–8
[39] Zhang M, Dobriyal P, Chen J-T, Russell T P, Olmo J and Merry A 2006 Wetting transition in cylindrical alumina nanopores with polymer melts *Nano Lett.* **6** 1075–9
[40] Martín J and Mijangos C 2008 Tailored polymer-based nanofibers and nanotubes by means of different infiltration methods into alumina nanopores *Langmuir* **25** 1181–7
[41] Tan A W and Torkelson J M 2016 Poly (methyl methacrylate) nanotubes in AAO templates: designing nanotube thickness and characterizing the T g-confinement effect by DSC *Polymer* **82** 327–36
[42] Martín J, Maiz J, Sacristan J and Mijangos C 2012 Tailored polymer-based nanorods and nanotubes by template synthesis: from preparation to applications *Polymer* **53** 1149–66
[43] Mijangos C, Hernández R and Martín J 2016 A review on the progress of polymer nanostructures with modulated morphologies and properties, using nanoporous AAO templates *Prog. Polym. Sci.* **54** 148–82
[44] Sousa C, Leitao D, Proenca M, Ventura J, Pereira A and Araujo J 2014 Nanoporous alumina as templates for multifunctional applications *Appl. Phys. Rev.* **1** 031102
[45] Yang J *et al* 2014 Morphology defects guided pore initiation during the formation of porous anodic alumina *ACS Appl. Mat. Inter.* **6** 2285–91
[46] Hunter M and Fowle P 1954 Determination of barrier layer thickness of anodic oxide coatings *J. Electrochem. Soc.* **101** 481–5
[47] Keller F, Hunter M and Robinson D 1953 Structural features of oxide coatings on aluminum *J. Electrochem. Soc.* **100** 411–9
[48] Xia Y and Halas N J 2005 Shape-controlled synthesis and surface plasmonic properties of metallic nanostructures *MRS Bull.* **30** 338–48
[49] Giannini V, Fernández-Domínguez A I, Sonnefraud Y, Roschuk T, Fernández-García R and Maier S A 2010 Controlling light localization and light–matter interactions with nanoplasmonics *Small* **6** 2498–507
[50] Wang H, Brandl D W, Nordlander P and Halas N J 2007 Plasmonic nanostructures: artificial molecules *Acc. Chem. Res.* **40** 53–62
[51] Knight M W, King N S, Liu L, Everitt H O, Nordlander P and Halas N J 2013 Aluminum for plasmonics *ACS Nano* **8** 834–40
[52] Wu M, Wen L, Lei Y, Ostendorp S, Chen K and Wilde G 2010 Ultrathin alumina membranes for surface nanopatterning in fabricating quantum-sized nanodots *Small* **6** 695–9
[53] Scholl J A, Koh A L and Dionne J A 2012 Quantum plasmon resonances of individual metallic nanoparticles *Nature* **483** 421–7
[54] Gandra N and Singamaneni S 2012 Clicked plasmonic core-satellites: covalently assembled gold nanoparticles *Chem. Commun.* **48** 11540–2